Journal of Materials Science & Technology 34 (2018) 2271–2282

Contents lists available at ScienceDirect

Journal of Materials Science & Technology

journal homepage: www.jmst.org

Initial formation of corrosion products on pure zinc in simulated body fluid

Lijun Liu[a,1], Yao Meng[a,1], Chaofang Dong[a,b], Yu Yan[b], Alex A. Volinsky[c], Lu-Ning Wang[a,*]

[a] State Key Laboratory for Advanced Metals and Materials, School of Materials Science and Engineering, University of Science and Technology Beijing, Beijing, 100083, China
[b] Institute for Advanced Materials and Technology, University of Science and Technology Beijing, Beijing, 100083, China
[c] Department of Mechanical Engineering, University of South Florida, Tampa, FL, 33620, USA

ARTICLE INFO

Article history:
Received 12 January 2018
Received in revised form 25 February 2018
Accepted 13 March 2018
Available online 3 May 2018

Keywords:
Zinc
Stent
Corrosion
Simulated body fluid

ABSTRACT

Zinc was recently suggested to be a potential candidate material for degradable coronary artery stent. The corrosion behavior of pure zinc exposed to r-SBF up to 336 h was investigated by electrochemical measurements and immersion tests. The morphology and chemical composites of the corrosion products were investigated by scanning electron microscope, grazing-incidence X-ray diffraction, X-ray photoelectron spectroscopy and Fourier transform infrared spectrometer. The results demonstrate that the initial corrosion products on the pure zinc mainly consist of zinc oxide/hydroxide and zinc/calcium phosphate compounds. The pure Zn encounters uniform corrosion with an estimated corrosion rate of 0.02–0.07 mm y^{-1} during the immersion, which suggests the suitability of pure Zn for biomedical applications.

1. Introduction

Zinc (Zn) was recently suggested as a potential material for degradable coronary artery stents because of its biological merits and ideal degradation rate [1–3]. In human physiology, Zn is considered to be an essential trace element and takes part in many important biological reactions [4]. A major biological role of Zn is that it is closely regulated passage via channels within the cells wall. Once Zn has entered the cytoplasm, it plays many different roles, such as the regulation of DNA replication [5], apoptosis coordination [6], and metal-based enzymes [7]. The recommended dietary allowance (RDA) for Zn is 2 mg d^{-1} for infants, 11 mg d^{-1} for men and 8 mg d^{-1} for women [8]. Some *in vivo* tests reveal that Zn exhibited a strong antiatherogenic character [9], good hemocompatibility [10] along with non-cytotoxicity to endothelial cell [11].

Although Zn is one of the few physiologically relevant metallic elements, it had not received much research attention for application in biodegradable stents prior to 2011. It was shown that Zn degradation proceeds in rat's arteries at a rate of 0.01–0.02 mm y^{-1} [8], nearly identical to the 0.02 mm y^{-1} benchmark value for ideal bioabsorbable materials. However, due to its low tensile strength of <120 MPa [12], which is unacceptable for stent applications, Zn-based alloys with improved ductility, strength and corrosion uniformity have been introduced by several research groups [12–15]. In addition, it was suggested that by using Zn and its alloys, many of the core engineering problems associated with Mg and Fe could be avoided.

Corrosion behavior, including the corrosion rate measurement and formation of corrosion products, is crucial for understanding the basic corrosion processes underpinning absorption of biodegradable metals. However, to date, only a limited number of studies have been reported on the corrosion behavior of Zn in physiological conditions. Cheng et al. [11] compared the corrosion behavior of five pure metals including Zn by electrochemical measurement and static immersion test in Hank's solution. It is found that the corrosion rate of Zn was between Fe and Mn. Chen et al. [16] compared the corrosion behavior of pure Zn with Fe and Mg in phosphate buffered saline (PBS). They found that for transient assays, the corrosion rate placed Zn between Fe and Mg. However, in a long-term course the corrosion rate of Zn developed faster than Fe and Mg because of the unique localized corrosion.

* Corresponding author.
E-mail address: luning.wang@ustb.edu.cn (L.-N. Wang).
[1] These authors contributed equally to this work.

https://doi.org/10.1016/j.jmst.2018.05.005
1005-0302/

Liu et al. [17] studied the corrosion of ultra-pure Zn and its mini-tube in Hank's solution, which showed appropriate corrosion rate of 0.027–0.036 mm y^{-1}. Due to lack of suitable standard for corrosion evaluation of Zn-based biodegradable metals *in vitro*, some researches focused on the corrosion profiles of Zn in different corrosive medium. Törne et al. [18] researched the degradation of zinc in saline solutions, plasma, and whole blood. It was not possible to tell which solution was more appropriate to predict the degradation profile of Zn during clinical application. The corrosion mechanism of Zn *in vitro* is still unclear. Thus, in order to better understand the corrosion control of Zn, it is necessary to study its continuous corrosion process during the course of degradation.

Different artificial solutions mimicking the physiological environment, such as PBS, Hank's solution, Ringer's solution, revised simulated body fluid (r-SBF), and human plasma [18–25] have been used for *in vitro* tests. The concentrations of major components of the commonly used test media are listed in Table 1. Compared to whole blood, r-SBF has similar inorganic constituents other than cells and many organic molecules, such as amino acids and proteins. Thus, the r-SBF was selected in this *in vitro* study to simulate the blood plasma.

In order to elucidate the corrosion mechanism, pure Zn was chosen for the tests, with the aim to reduce the effects of other elements that might interfere with the interpretation of the degradation behavior of the matrix. The corrosion behavior of pure Zn immersed in r-SBF was investigated in the present work to provide more details regarding the corrosion processes and mechanisms of pure Zn. This fundamental understanding of *in vitro* study will pave the way for potential biomedical applications.

2. Experimental

2.1. Sample preparation

Zn with 99.99% purity was purchased from China New Metal Materials Technology Co.Ltd. The Zn samples were cut into 2 mm thick discs with a 10 mm diameter. Samples were mechanically ground with silicon carbide sandpapers, polished with diamond abrasive paste, followed by ultrasonic rinsing in milli-Q water, acetone and ethanol successively to remove surface contaminants. The samples were then dried and stored in a vacuum.

2.2. Electrochemical measurements

Electrochemical measurements, including potentiodynamic polarization (PDP) test and electrochemical impedance spectroscopy (EIS), were performed by an electrochemical analyzer (ModuLab XM). A three electrode cell set-up was used wherein the pure Zn samples, saturated calomel electrode (SCE) and a platinum sheet (1 cm × 1 cm) were used as the working, reference and counter electrodes, respectively. For the working electrode, the backside of the samples was connected with a copper wire and then sealed with epoxy to expose the research surface area of 1 cm^2. A stable open circuit potential was established prior to all tests. The potentiodynamic polarization tests were carried out at a constant scan rate of 1 mV s^{-1}, initiating from −1.4 V_{SCE} to −0.5 V_{SCE}. The corrosion potential E_{corr}, corrosion current density I_{corr}, and cathodic Tafel slopes β_c were determined by the Tafel linear extrapolation of the cathodic branches with an over potential of ca. 50 mV. An average of three samples was taken for each group and new samples with corrosion products were prepared for every time point. EIS studies were carried out at open circuit potential of 10 mV sinusoidal amplitude over 100 kHz to 10 m Hz frequency range. Four samples were immersed in the r-SBF and taken out at specific time intervals for the EIS test. The impedance data were analyzed with the ZSimpWin software package and fitted to the equivalent curves. All experiments were conducted at 37 ± 0.1 °C in r-SBF (NaCl 8.035 g L^{-1}, KCl 0.225 g L^{-1}, $NaHCO_3$ 0.355 g L^{-1}, $K_2HPO_4{\cdot}3H_2O$ 0.231 g L^{-1}, $MgCl_2{\cdot}6H_2O$ 0.311 g L^{-1}, $CaCl_2$ 0.292 g L^{-1} and Na_2SO_4 0.072 g L^{-1}).

2.3. Immersion tests

The corrosion behavior tests of Zn samples were carried out by *in vitro* immersion in r-SBF. The pH was adjusted to 7.4 by adding appropriate amount of tris(hydroxymethyl) aminomethane buffer (Tris-HCl). The samples were soaked in the solution with a volume-to-sample area ratio of 20 mL cm^{-2}. Then the samples were immersed in 40 mL r-SBF at 37 °C. During the immersion, the pH values of r-SBF were determined by the FE 20 pH meter (Mettler Toledo). The amount of released zinc ions into the r-SBF was evaluated using an atomic absorption spectrophotometer (AAS, Thermo Scientific M Series). In order to assess the corrosion behavior and the corrosion product formation during the initial degradation stage, the samples soaking up to 336 h were taken out at different temporal intervals and investigated. For different time intervals, the corrosion products on the sample surfaces were removed in the chemical cleaning solution according to ISO 8407 [26]: 100 g/L NH_4Cl for 2–5 min at 70 °C. Afterwards, the samples were rinsed by ethanol and dried before being weighed. The weight loss (mg cm^{-2}) was calculated using the following equation [27]:

$$\text{weightloss} = (m_i - m_f)/A \quad (1)$$

where m_i is the initial weight of the sample before immersion (mg), m_f is the final weight of each sample after immersion (mg), and A is the sample surface area exposed to r-SBF (cm^2). In addition, the corrosion rate derived from weight loss (CR_w, mm y^{-1}) of pure Zn can be calculated by the following equation according to ASTM G31-72 [28]:

$$CR_w = 87.4 \times (m_i - m_f)/(ADt) \quad (2)$$

where m_i is the initial weight of the sample before immersion (mg), m_f is the final weight of each sample after immersion (mg), A is the exposed area (cm^2); D is the alloy density (g cm^{-3}); and t is the immersion time (h).

2.4. Characterization of corrosion products

Surface morphology of Zn samples after immersion was investigated using a scanning electron microscope (SEM, FEI Quanta 200) coupled with an Oxford Instrument INCA X-max^N-sight EDX analyzer. X-ray photoelectron spectroscopy (PHI 5600 XPS spectrometer) was used to characterize the surface chemical states of samples after immersion. The XPS spectra were recorded using AlK_α radiation (1486.6 eV) as excitation source. The chemical groups of the corrosion products were characterized by Fourier transform infrared spectrometer (FTIR, Nicolet 5700) in the 4000–600 cm^{-1} wave number range. Grazing-incidence X-ray diffraction (GIXRD) measurements were conducted on the Smart Lab X-ray diffractometer (Rigaku) with CuK_α radiation at an incident angle of 0.1° to determine the structure of the coatings. The XRD spectra were collected at angles between 10° and 90° at a rate of 0.02° s^{-1}. Reference standards from the Joint Committee on Powder Diffraction Standards (ICDD-JCPDS) database were used to identify the various compounds of the corrosion layer.

Table 1
Comparison of the inorganic ion concentrations and some organic components among human blood plasma, r-SBF, PBS, Ringer's solution and Hank's solution.

	Plasma [24]	r-SBF [19]	PBS [20,21]	Ringer's solution [22]	Hank's Solution [23,25]
Na^+ (mmol/L)	142.0	142.0	154.05	156.4	141.8
K^+ (mmol/L)	5.0	5.0	4.14	5.8	5.8
Ca^{2+} (mmol/L)	2.5	2.5	–	2.2	2.5
Mg^{2+} (mmol/L)	1.5	1.5	–	–	0.8
Cl^- (mmol/L)	103.0	103.0	140.6	164.2	147.4
HCO_3^- (mmol/L)	27.0	27.0	–	2.4	4.2
HPO_4^{2-} (mmol/L)	1.0	1.0	8.06	–	0.3
$H_2PO_4^-$ (mmol/L)	–	–	1.47	–	0.4
SO_4^{2-} (mmol/L)	0.5	0.5	–	–	0.8
Amino acids (mg/L)	nd	–	–	–	
Glucose (g/L)	nd	–	–	–	5.6
Proteins (g/L)	63–80	–	–	–	

nd: no data available.

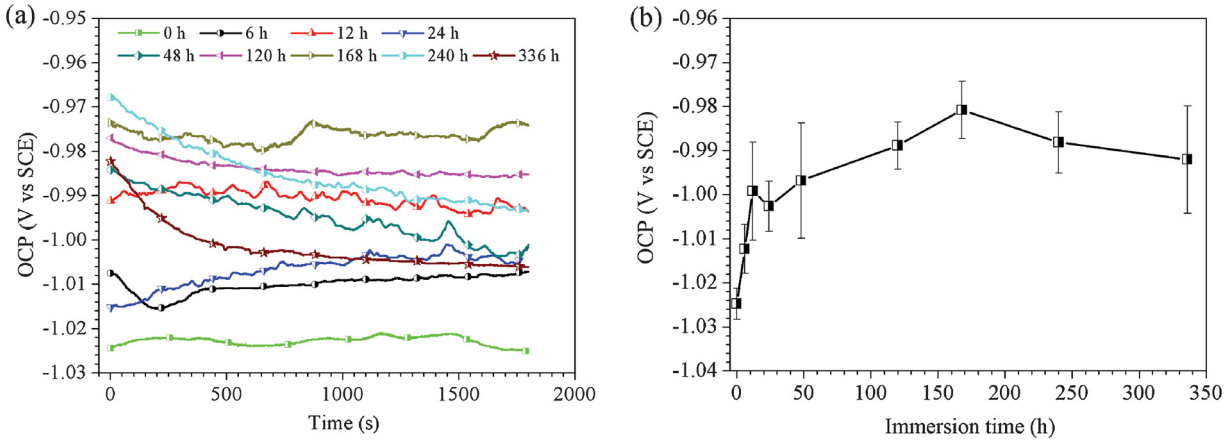

Fig 1. (a) OCP with respect to time of pure Zn at different immersion periods in r-SBF and (b) OCP of pure Zn as a function of immersion time.

3. Results

3.1. Electrochemical measurements

3.1.1. Open circuit potential

As shown in Fig. 1(a), after different immersion periods, the open circuit potential (OCP) values underwent frequent variations throughout the tests. The evolution of OCP, the values at which the EIS measurement was carried out, was summarized in Fig. 1(b). It was obvious that all the OCP values after immersion were higher than that at 0 h due to the formation of corrosion products in the course of immersion. It also can be seen that the OCP values for 48 h, 240 h and 336 h decreased gradually, the trends of which were different from other curves. The phenomena may be attributed to the breakdown of the corrosion products on sample surfaces. The variations of OCP at different immersion period indicated the constant change in composition or morphology of the sample surfaces.

3.1.2. Potentiodynamic polarization test

Fig. 2(a) shows the PDP curves of pure Zn after immersion in r-SBF for different amount of time. The anodic branches showed nearly the same trend with the exception of 0 h and 6 h, which revealed passivation-like regions and acceleration to high dissolution rate. The cathodic domain included an almost vertical stage up to −1.2 V_{SCE} and a slope region (mainly ranging from −1.2 V_{SCE} to corrosion potential), which were corresponding to hydrogen generation process and the oxygen consumption process, respectively [16,29]. The related parameters, E_{corr}, I_{corr} and β_c, obtained from the PDP curves were shown in Table 2. The *E*corr values of pure Zn did not change much as the immersion evolves. Neertheless, the

Table 2
The polarization data of the pure Zn at different immersion periods in r-SBF.

Immersion time	E_{corr} (V vs. SCE)	I_{corr} (μA cm^{-2})	β_c (V dec)
0 h	−1.12 ± 0.09	5.72 ± 6.77	0.13 ± 0.07
6 h	−1.02 ± 0.04	2.55 ± 1.03	0.15 ± 0.04
12 h	−0.99 ± 0.01	4.25 ± 1.67	0.15 ± 0.21
24 h	−1.03 ± 0.0002	6.03 ± 2.35	0.17 ± 0.05
48 h	−1.01 ± 0.01	18.90 ± 5.83	0.29 ± 0.06
120 h	−1.04 ± 0.03	11.30 ± 3.52	0.28 ± 0.10
168 h	−0.98 ± 0.02	5.77 ± 3.47	0.13 ± 0.04
240 h	−0.99 ± 0.02	18.00 ± 2.07	0.19 ± 0.09
336 h	−1.08 ± 0.07	11.90 ± 4.29	0.22 ± 0.08

*I*corr values frequently fluctuated during the immersion, which can be seen clearly in Fig. 2(b).

3.1.3. EIS measurement

Fig. 3(a) portrayed the Bode plots of pure Zn at different time point. Two peaks were clearly observed at high and low frequency, indicating the existence of two time constants. In order to clarify the corrosion resistance of pure Zn after different immersion time, the equivalent electrical circuit (EEC) was applied to fit the EIS results. As shown in Fig. 3(b), *R*s was the solution resistance, R_{ct} and Q_{dl} represented the resistance of charge transfer and capacitance of the electrical double layer; *Q* was used here in place of a capacitor to compensate for the non-homogeneity of the system [30–32]. R_c and C_c represented the resistance and capacitance of corrosion product layer. Both fitted parameters were summarized in Table 3. R_s value was almost the same due to the same solution used in the test. The R_c and R_{ct} of pure Zn displayed the same trend that decreased within 24 h, then increased gradually to 168 h and decreased again afterwards. As reported by Heakal et al. [33], the

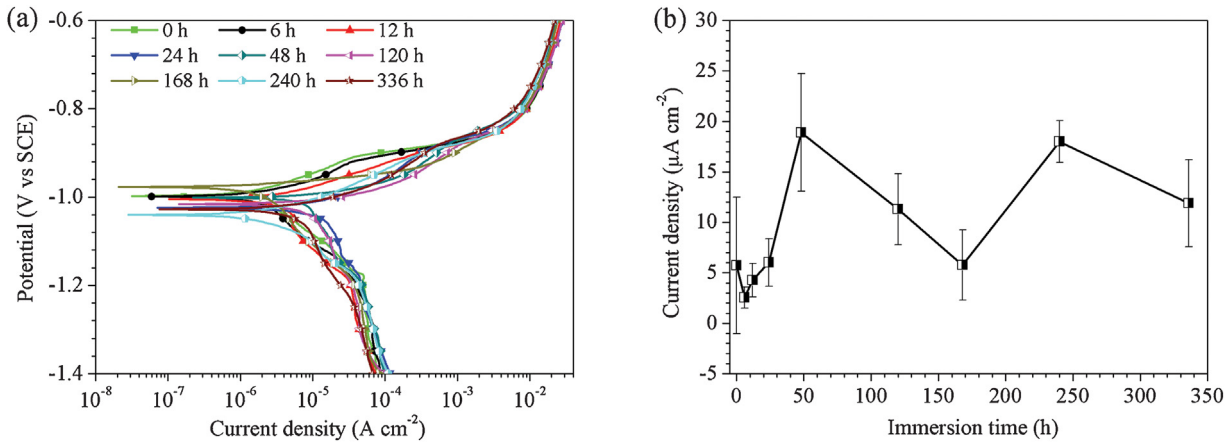

Fig. 2. (a) Potentiodynamic curves of pure Zn at different immersion periods in r-SBF: 0 h, 6 h, 12 h, 24 h, 48 h, 120 h, 168 h, 240 h and 360 h; (b) The current density obtained from PDP curves.

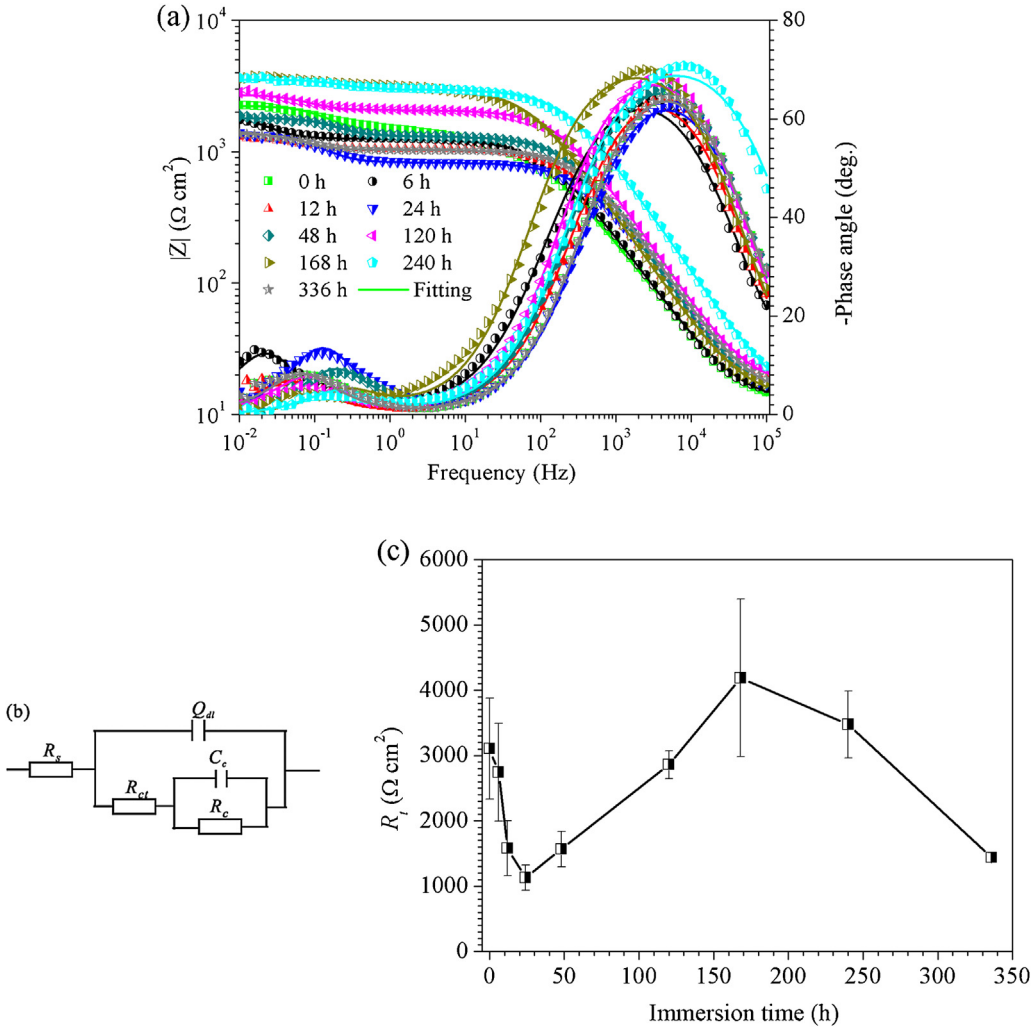

Fig. 3. EIS results of pure Zn after immersion in r-SBF: (a) Bode plots of |*Z*| vs. frequency and phase angle vs. frequency; (b) the equivalent electrical circuit used to fit the EIS data and (c) the total resistance R_t calculated from EIS components. Different immersion periods: 0 h, 6 h, 12 h, 24 h, 48 h, 120 h, 168 h, 240 h and 336 h. Symbols represent experimental data and lines represent simulated spectra.

total resistance value R_t, given by $R_t = R_c + R_{ct}$, can be used to evaluate the corrosion resistance of the samples. Fig. 3(c) depicted the trend of R_t. A distinction of the corrosion trend from the PDP and EIS was observed (Figs. 2(b) and 3(d)), which was likely caused by the different excitation over the samples [34].

3.2. Characterization of corrosion products

3.2.1. Surface morphology and chemical composition

Optical images of pure Zn taken from different immersion times are shown in Fig. 4. All samples still showed metallic luster after

Table 3
Equivalent electrical circuit parameters of the pure Zn at different immersion periods in r-SBF at 37 °C.

Immersion time	R_s (Ω cm^2)	Q_{dl} ($\mu\Omega^{-1}$ s^{-1} cm^{-2})	n	R_{ct} (Ω cm^2)	C_c (μF cm^{-2})	R_c (Ω cm^2)
0 h	12.17 ± 1.99	4.87 ± 2.00	0.79 ± 0.04	1962.67 ± 476.05	2530 ± 2880	1144.43 ± 297.76
6 h	12.70 ± 0.86	2.83 ± 0.97	0.81 ± 0.01	1765.33 ± 462.59	6910 ± 5480	977.03 ± 293.65
12 h	14.23 ± 0.31	2.02 ± 0.09	0.84 ± 0.01	1181.87 ± 338.15	2022 ± 1966	398.67 ± 108.17
24 h	13.96 ± 1.67	1.86 ± 0.09	0.83 ± 0.03	764.47 ± 93.07	1930 ± 1030	364.8 ± 120.54
48 h	13.08 ± 1.25	1.32 ± 0.37	0.83 ± 0.005	1174.93 ± 171.90	4250 ± 3690	390.67 ± 104.21
120 h	15.03 ± 2.07	1.32 ± 0.20	0.85 ± 0.006	2362.33 ± 260.53	1780 ± 1610	497.83 ± 157.23
168 h	14.00 ± 0.86	1.87 ± 0.19	0.84 ± 0	3442.33 ± 1087.38	820 ± 330	746.13 ± 169.88
240 h	12.79 ± 2.04	3.96 ± 3.51	0.84 ± 0.01	2733.67 ± 619.95	1350 ± 350	742.17 ± 185.11
336 h	13.58 ± 1.66	1.90 ± 1.14	0.82 ± 0.05	1092.17 ± 185.01	5240 ± 2390	347.17 ± 129.61

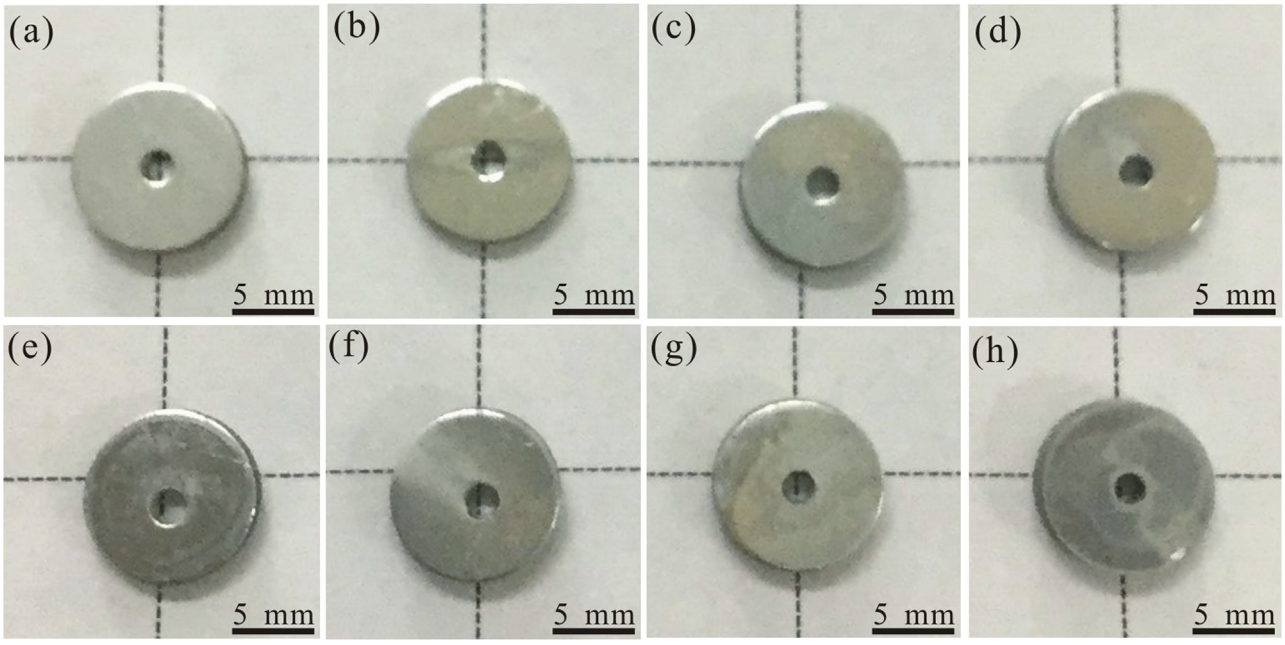

Fig. 4. Optical images of pure Zn tested in r-SBF for different time: (a) 6 h, (b) 12 h, (c) 24 h, (d) 48 h, (e) 120 h, (f) 168 h, (g) 240 h and (h) 336 h.

immersion up to 168 h (Fig. 4(a–f)). With the extension of immersion time, the sample surfaces were partially covered by whitish precipitates (Fig. 4(g and h)), which could be attributed to the precipitation of corrosion products during immersion. Besides, the surfaces did not exhibit significant changes and there was no sign of severe corrosion during the immersion.

Fig. 5 portrays the SEM images of pure Zn after immersion in r-SBF up to 336 h. The sample surface did not show any obvious change during the initial immersion stage from 6 h to 24 h, although the magnified micrographs in Fig. 5(a–c) showed that many nanoscale particles grew up unceasingly on the surface during the immersion. The globular corrosion products can be viewed scattered over the surface after immersion in r-SBF for 48 h (Fig. 5(d)). The growth of the spheroidal corrosion products upon immersing in r-SBF for 120 h was apparent in Fig. 5(e). Additionally, the precipitates aggregated when the immersion time was prolonged to 168 h (Fig. 5(f)). There was a primary layer of corrosion products, over which further growth of the spheroidal cluster proceeded in Fig. 5(d–f). With longer immersion time, the entire surface was covered by the spheroid structures and abundant clusters can be observed on the samples (Fig. 5(g and h)).The corresponding energy dispersive X-ray spectrometer (EDS) analysis of the samples after immersion in r-SBF for different time is listed in Table 4. It was evident that the dominant elements on sample surfaces were Zn, O, C and P, and trace amounts of Ca. With the immersion time extension, the atomic ratio of P to Zn increased significantly from 0.011 to 0.565, and the Ca content increased from 0.003 to 0.04.

Table 4
EDS data of the surface of Zn samples after immersion in SBF for different time (at.%).

	6 h	12 h	24 h	48 h	120 h	168 h	240 h	336 h
Zn	65.8	64.9	63.4	62.8	46.3	47.8	41.4	17.4
C	23.1	23.9	24.3	23.1	29.3	26.7	31.7	12.5
O	9.6	9.8	10.9	12.2	19.3	21.3	21.8	58.4
P	1.4	0.9	1.1	1.3	3.8	2.8	3.4	8.5
Ca	0.1	0.5	0.4	0.6	1.3	1.4	1.7	3.2
P/Zn	0.021	0.014	0.017	0.021	0.082	0.058	0.082	0.488

It can be deduced that the corrosion products mainly consisted of zinc oxide/hydroxide and zinc/calcium phosphate compounds. With increasing immersion time detectable species containing calcium and phosphate formed on the sample surfaces.

In order to investigate the corrosion propagation along the depth, SEM images and EDS line profiles were acquired from the cross-sectional observation of the Zn samples immersed for 120 h and 240 h. As shown in Fig. 6(a), a thin layer (~0.5 μm) was formed on the sample surface after immersion for 120 h and the corrosion layer became compact and the thickness was about 2.7 μm after immersion for 240 h (Fig. 6(c)). According to the EDS line scan profiles, it can be observed that the corrosion product layer consisted of Zn, P, Ca and O, which could be assigned to the formation of zinc oxide/hydroxide and zinc/calcium phosphate during immersion (Fig. 6(b and d)). It was evident that the intensity of the Zn signal from the corrosion layer becomes weaker than from the substrate because Zn dissolved during the immersion and formed

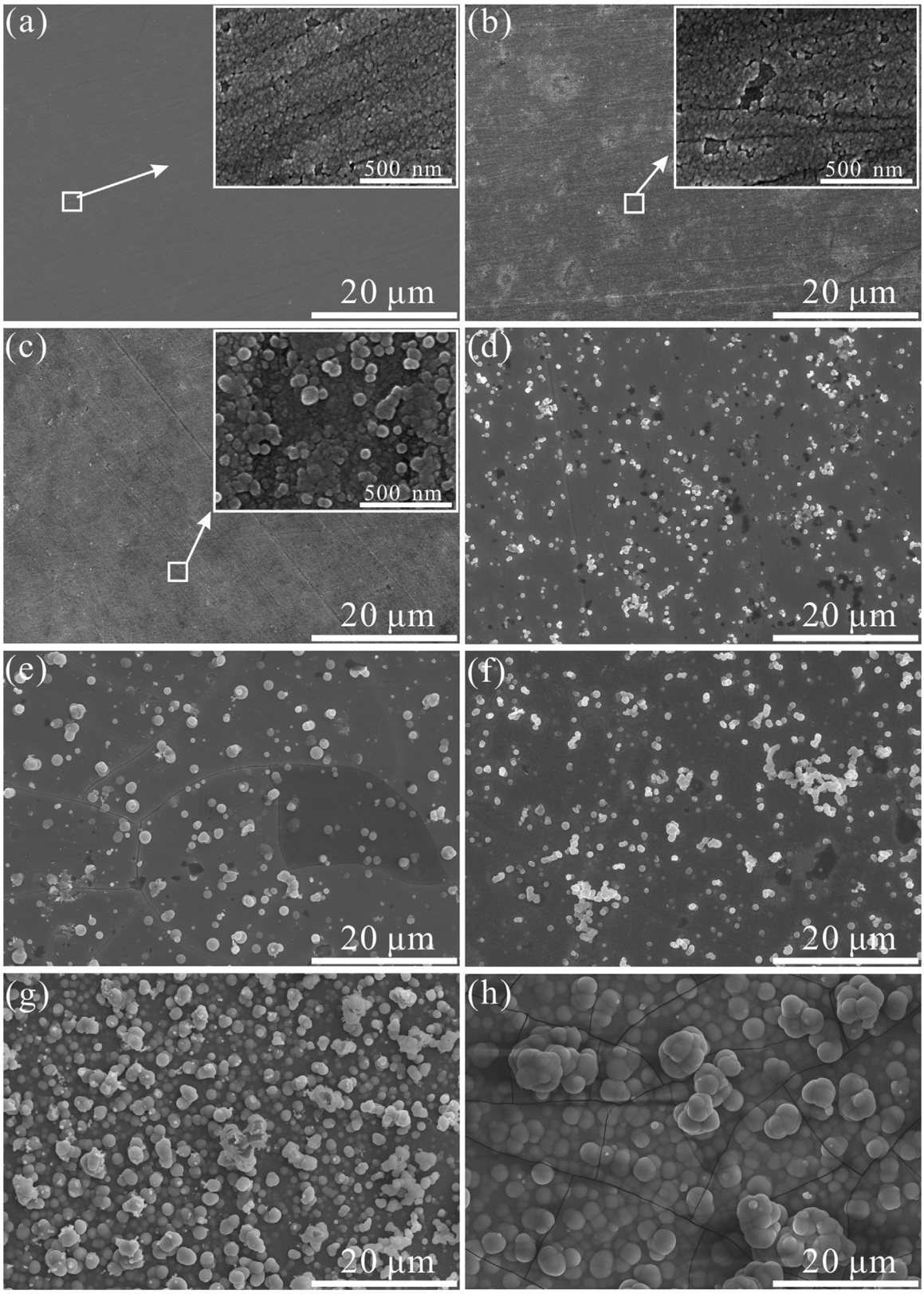

Fig. 5. SEM images of pure Zn immersed in r-SBF for (a) 6 h, (b) 12 h, (c) 24 h, (d) 48 h, (e) 120 h, (f) 168 h, (g) 240 h and (h) 336 h. The insets show local high magnification area.

corrosion products with other elements near the surface. Besides, the intensity of Ca and P signals became strong after immersion for 240 h (Fig. 6(d)). The EDS analysis suggested that the corrosion of Zn proceeds gradually in r-SBF. Meanwhile, calcium phosphate precipitated continuously on the sample surface with longer immersion time.

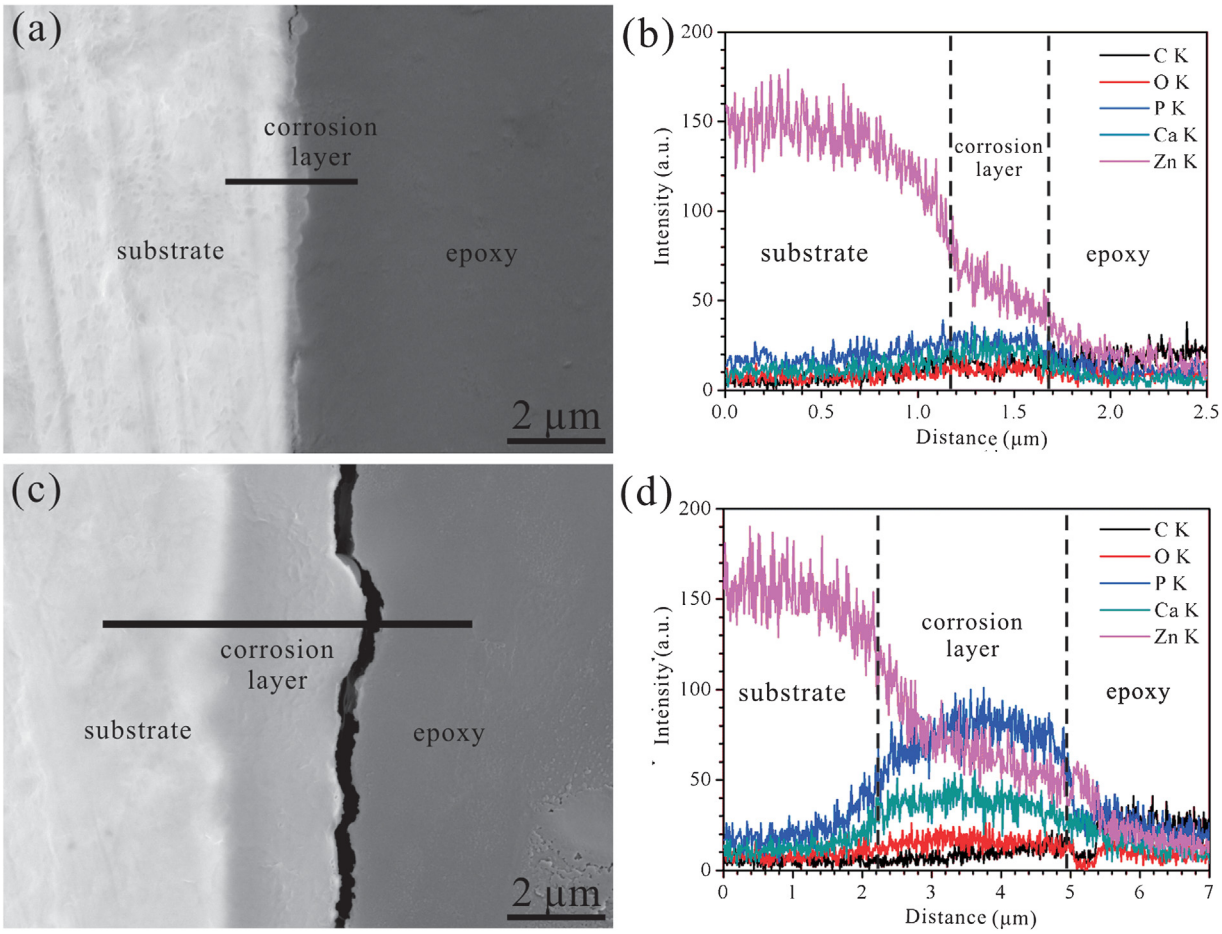

Fig. 6. Cross-sectional images and EDS line profile of pure Zn immersed in r-SBF for (a, b) 120 h and (c, d) 240 h.

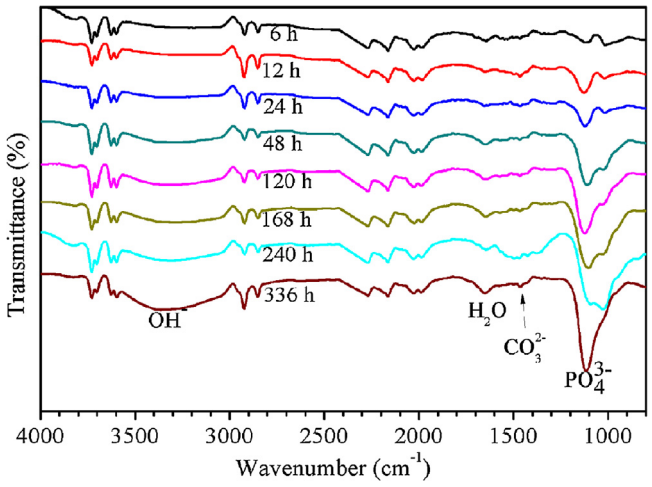

Fig. 7. FTIR spectra of Zn sample surfaces after immersion in r-SBF for 6 h, 12 h, 24 h, 48 h, 120 h, 168 h, 240 h and 336 h.

3.2.2. FTIR analysis

Fig. 7 displays the FTIR spectra of pure Zn sample immersed in r-SBF for different time. The broad absorption from 3600 to 3100 cm^{-1} was attributed to the O—H stretching vibration of the hydroxyl group [35]. The peak at 1640 cm^{-1} was attributed to H_2O bending vibration [35] and rotation modes manifested the existence of crystal water [36]. Weak peaks between 1470 and 1420 cm^{-1} were assigned to the stretching vibration of some absorbed carbonate ions from the solution [37,38]. The peaks at 1100 and 1025 cm^{-1} were assigned to the P—O asymmetric stretching vibration of phosphate [39,40], which became stronger with prolonging the immersion time to 336 h. These results indicated that more phosphates formed on the Zn sample surfaces with extended soaking time, which verified the presence of phosphate species in the corrosion products.

3.2.3. XPS analysis

The XPS analysis results of pure Zn after immersion for different time are displayed in Fig. 8. Fig. 8(a) shows the XPS survey of all samples. Compared to the pure Zn before immersion, new peaks of P 2*p* and Ca 2*p* were detected on the samples shortly after immersion in r-SBF for 6 h. These results revealed that the corrosion products mainly consisted of Zn, O, Ca, P and C elements. There was no significant difference in chemical composition of the corrosion products after different immersion time. In order to obtain detailed information about the corrosion products, high resolution XPS data for P 2*p* and Zn $2p_{3/2}$ were also collected.

The P 2*p* spectra are depicted in Fig. 8(b). It was obvious that the P 2*p* peaks shift towards low binding energy after 120 h immersion, which can be explained by the changes of corrosion products with immersion. As seen in Fig. 8(d–g), the observed peaks were decomposed into three contributions located at 133.93 eV, 133.50 eV and 133.20 eV, which are associated with $Zn_3(PO_4)_2$ [41], $CaHPO_4{\cdot}2H_2O$ [42] and $Ca_3(PO_4)_2$ [43], respectively. The proportion of the components in the corrosion products were listed in Table 5. With

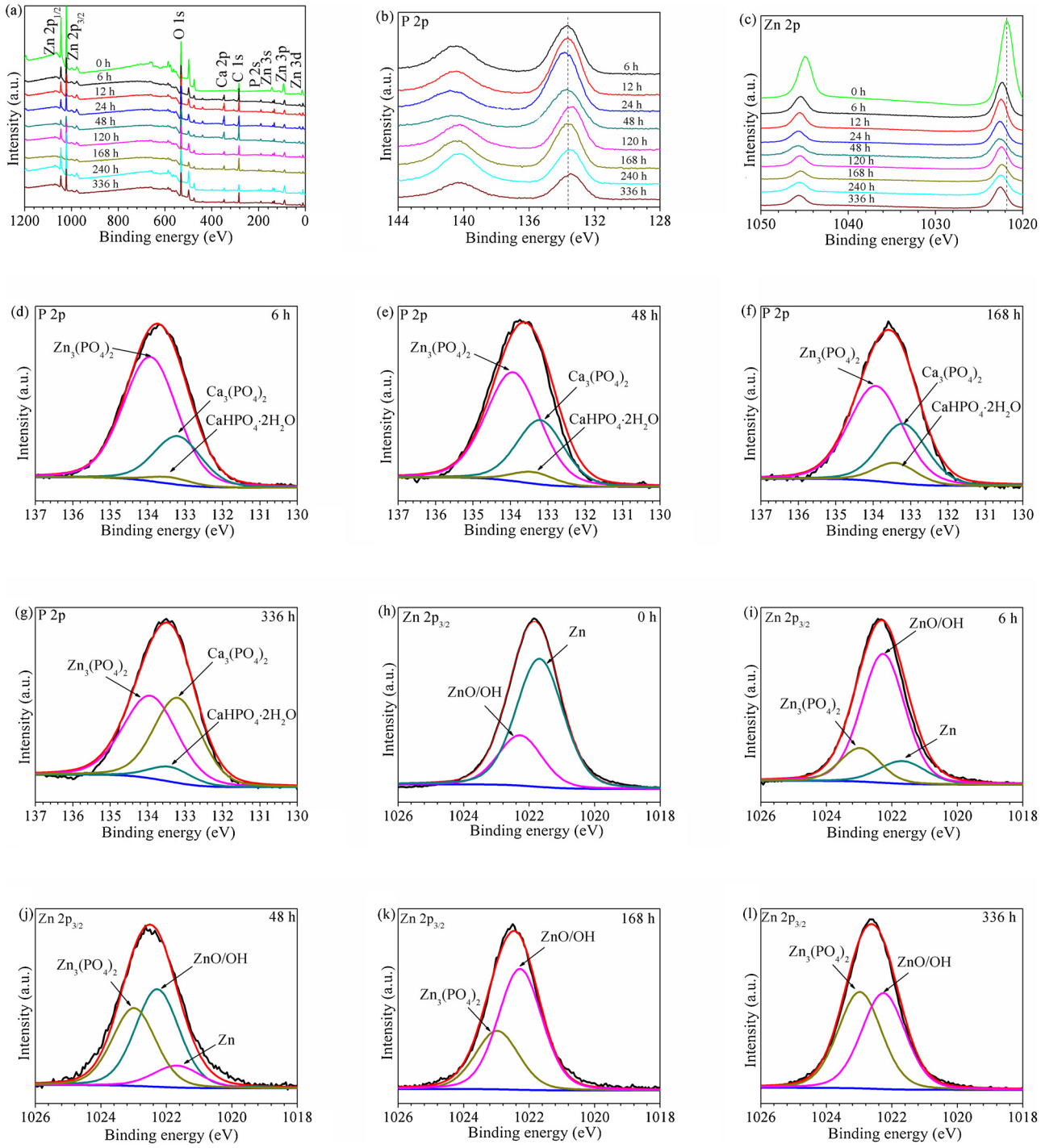

Fig. 8. XPS spectra of pure Zn: (a) The overview XPS spectrum, (b) P 2p and (c) Zn $2p_{3/2}$ spectra of pure Zn after immersion in r-SBF for 6 h, 12 h, 24 h, 48 h, 120 h, 168 h, 240 h and 336 h; Deconvoluted XPS spectra (d–g) of P 2p after immersion for 6 h, 48 h, 168 h and 336 h, and (h–l) of Zn $2p_{3/2}$ after immersion for 0 h, 6 h, 48 h, 168 h and 336 h.

Table 5
Proportion of different component in the corrosion products (%).

Immersion time	$Zn_3(PO_4)_2$	$Ca_3(PO_4)_2$	$CaHPO_4{\cdot}2H_2O$
6 h	72.2	24.8	3.0
48 h	62.5	32.3	5.2
168 h	58.2	36.2	5.6
336 h	49.0	44.2	6.8

the extension of immersion time, the proportion of $Zn_3(PO_4)_2$ decreased gradually from 72.2 to 49.0, whilst the increment of $Ca_3(PO_4)_2$ and $CaHPO_4{\cdot}2H_2O$ were obviously detected. This result suggested the successive accumulation of calcium phosphate compounds on the sample surfaces.

Fig. 8(c) demonstrates the Zn $2p_{3/2}$ spectra of pure Zn as functions of the immersion time. The peak intensity decreased significantly after immersion and the changes in binding energy were clearly observed with time. The spectra were decomposed using two contributions attributed to $ZnO/Zn(OH)_2$ and Zn located at 1022.26 eV [44] and 1021.68 eV [45], respectively (Fig. 8(h)). Additionally, a new peak associated with $Zn_3(PO_4)_2$ was present at 1022.99 eV [46], and coexisted with $ZnO/Zn(OH)_2$ species during further immersion (Fig. 8(i–l)). The intensity of Zn gradually

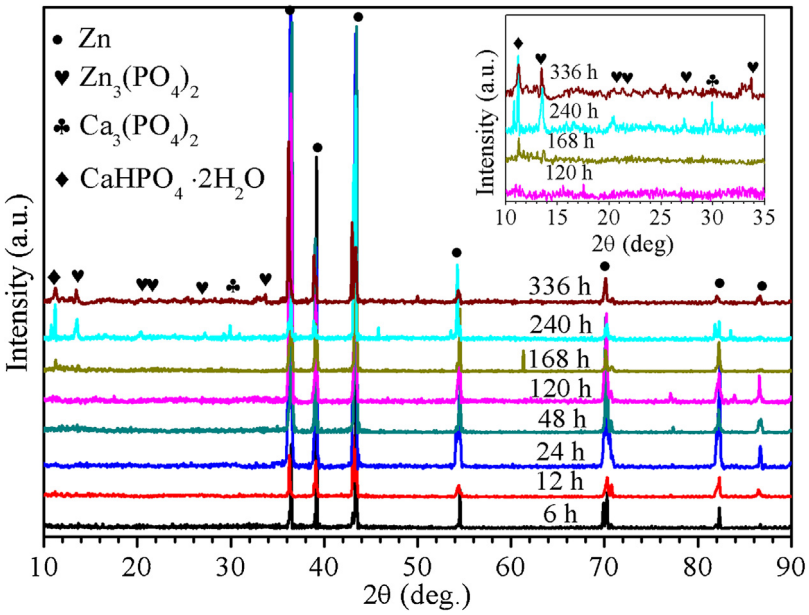

Fig. 9. GIXRD patterns of Zn after immersion in r-SBF solution for 6 h, 12 h, 24 h, 48 h, 120 h, 168 h, 240 h and 336 h. Inset shows the high magnification patterns from 10° to 38° 2θ angle for Zn immersed for 120 h, 168 h, 240 h and 336 h.

decreased in the initial immersion and was hardly detected after 168 h (Fig. 8(k)). In contrast, the proportion of $Zn_3(PO_4)_2$ increased gradually from 17% for 6 h to 50.1% for 336 h. These results confirmed the presence of ZnO/$Zn(OH)_2$ and $Zn_3(PO_4)_2$ in the corrosion products.

3.2.4. XRD analysis

The GIXRD patterns of the samples after exposure to r-SBF solution for different time are displayed in Fig. 9. In addition to the dominant peaks corresponding to the Zn phase, a number of peaks with low intensity for Zn3(PO4)2, Ca3(PO4)2 and CaHPO4·2H2O were detected on the samples after immersion for 168 h. Peaks of ZnO or Zn(OH)2 were absent, possibly attributed to their low contents, which cannot be detected by XRD.

3.3. Immersion test

3.3.1. pH assessment, dissolution and weight loss studies

The pH values of r-SBF as a function of immersion time are shown in Fig. 10(a). A linear increase in pH of the r-SBF solution was found during the initial immersion up to 96 h. Afterwards a slow increase of pH was observed by further immersion from 96 h to 240 h. And then a relatively constant pH value of 7.63 was detected. As depicted in Fig. 10(b), the release rate of Zn^{2+} was fast within the 72 h immersion and became slow during further immersion. After 312 h, the accumulated Zn^{2+} release was about 40 mg L^{-1}. As shown in Fig. 10(c), the weight loss of Zn samples increased steadily with time and reached 1.64 mg cm^{-2} after 336 h, ascertaining the perpetual corrosion of pure Zn in the r-SBF.

3.3.2. Micrograph of corroded Zn sample

Fig. 11 provides representative SEM images of pure Zn immersed for 48 h and 336 h after removal of the corrosion products to unveil the underneath corrosion attack. After different immersion intervals, Zn samples showed uniform corrosion and no obvious localized corrosion pits were detected, except shallow scratches caused by the polishing procedure.

Table 6
Corrosion rates of pure Zn in the r-SBF obtained from the electrochemical measurements (CR_i, mm y^{-1}) and immersion tests (CR_w, mm y^{-1}).

Immersion time	CR_i (mm y^{-1})	CR_w (mm y^{-1})
0 h	0.08 ± 0.10	0
12 h	0.06 ± 0.02	0.04 ± 0.02
24 h	0.09 ± 0.03	0.06 ± 0.01
48 h	0.28 ± 0.09	0.05 ± 0.006
120 h	0.17 ± 0.05	0.04 ± 0.006
168 h	0.09 ± 0.05	0.03 ± 0.006
240 h	0.27 ± 0.03	0.03 ± 0.001
336 h	0.18 ± 0.06	0.03 ± 0.002

4. Discussion

4.1. Corrosion rate of zinc in r-SBF

Table 6 summarized the corrosion rates of pure Zn calculated from the PDP curves and immersion tests. The corrosion rate CR_i (mm y^{-1}) converted from the current density I_{corr} (μA cm^{-2}) is expressed as follows [47]:

$$CR_i = 315.36 \times aI_{corr}/(nFD) \quad (3)$$

where a is the atomic weight (g mol^{-1}); n is number of equivalent exchange; F is the Faraday's constant (coulombs mol^{-1}) and D is the alloy density (g cm^{-3}).

The value of CR_i fluctuated throughout the immersion as the I_{corr} values in Fig. 2(b). Nevertheless, the CR_w gradually increased and became relatively steady after 168 h during the immersion test. The CR_w of pure Zn was estimated to be 0.02–0.07 mm y^{-1}, which was similar to the results *in vitro* reported by Vojtěch et al. [48] and Tang et al. [49]. As listed in Table 6, the CR_i value in each immersion period was almost 2–10 times higher than the CR_w obtained from the immersion tests. It should be noted that corrosion rates derived from the PDP curves only provide the rate at the specific temporal stage but the ones calculated from immersion tests are accumulative values during the immersion. Whilst electrochemical test is a powerful method for revealing the dominant mechanisms (i.e. anodic or cathodic reaction changes), the results depicted a

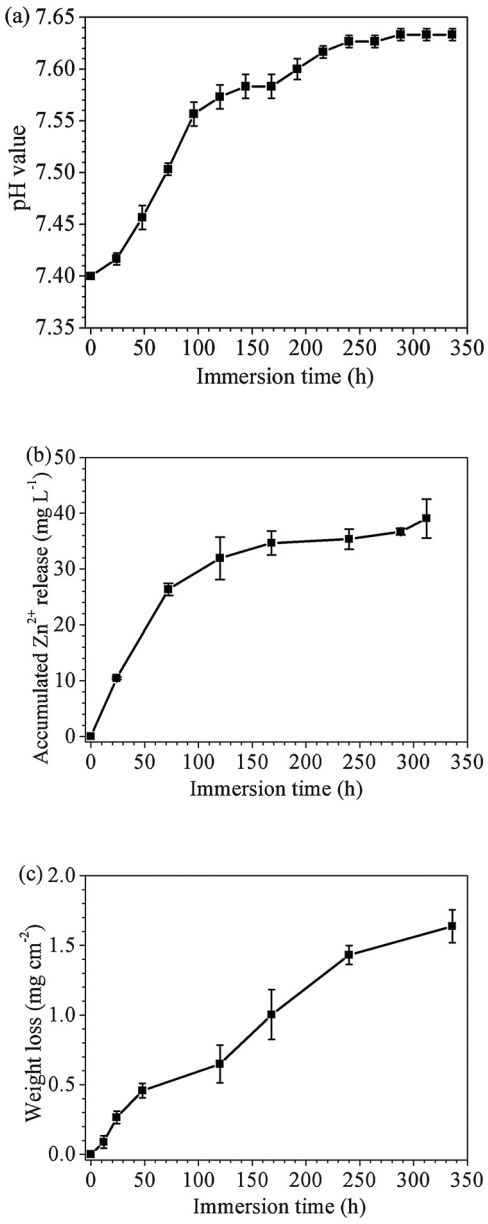

Fig. 10. (a) pH vibration in r-SBF, (b) accumulated Zn^{2+} ion and (c) weight loss vibration of immersed Zn samples as a function of immersion time.

specific moment in the corrosion process. The immersion test is still necessary to evaluate the degradation behavior for the samples.

4.2. Corrosion mode of zinc in r-SBF

Although some previous results [11,16] demonstrated that localized corrosion was observed on pure Zn with different purities during immersion in Hank's solution or PBS, in the present study pure Zn encountered uniform corrosion after immersion in r-SBF for 336 h as shown in Fig. 11. The different components of the corrosive medium (listed in Table 1) played an important role in the corrosion behavior of the samples. Moreover, the scratches on Zn samples after grinding with SiC papers can be viewed as surface defects vulnerable to the corrosive solution. Whilst the Zn samples used in present study were polished by diamond paste. The corrosion mode of pure Zn could also be affected by the initial surface conditions [50].

In view of assessing the value of this research, data from pure Mg were supplied for comparison. As reported by other researchers [51–53], the pH increased rapidly as soon as pure Mg immersed in SBF. However, the pH value for the pure Zn gradually increased during the initial immersion and then maintained itself at 7.63, which was also lower than the corresponding value of pure Mg. The slight increase in the pH value could have a mild influence on local physiological conditions [8]. On the other hand, pure Mg generally encountered severe pitting corrosion in the simulated fluids, while pure Zn showed uniform corrosion (Fig. 11). The rapid corrosion rate of pure Mg also has an adverse effect on the mechanical property, leading to the early failure of sufficient support. The pure Zn displayed appropriate corrosion rate, near to the ideal value for bioabsorbable materials. It was likely that pure Zn was more suitable to be used as biomedical materials from the corrosion perspective.

In view of the discrepancies between *in vitro* and *in vivo* test conditions, some researches on the degradation of pure Zn *in vivo* were introduced here. Bowen et al. [3] found that after 6 months, the corrosion products on Zn wires mainly consisted of ZnO and zinc carbonate with Ca/P phase on the exterior surface. The corrosion rate of pure Zn *in vivo* was 0.02–0.05 mm y^{-1}. Yang et al. [54] implanted zinc wires into the abdominal aorta of rabbits for 12 months. The zinc wires displayed uniform corrosion mode in the initial stages and localized corrosion after endothelialization. The degradation product was zinc phosphate at first and then transformed into zinc oxide and small amounts of calcium phosphate. The average penetration rates were within the range of 10–30 mm y^{-1}. Drelich et al. [55] conducted clinically relevant long-term *in vivo* studies to characterize the zinc implants biocorrosion behavior. They found that the zinc wires exhibited steady corrosion up to at least 20 months and that zinc oxide, zinc carbonate, and zinc phosphate were the main components of corrosion products surrounding the Zn implants. Compared with the aforementioned *in vivo* tests, the corrosion rates estimated in this work were near the data reported by Bowen et al. [3]. The pure Zn disks immersed in r-SBF displayed uniform corrosion, a behavior also

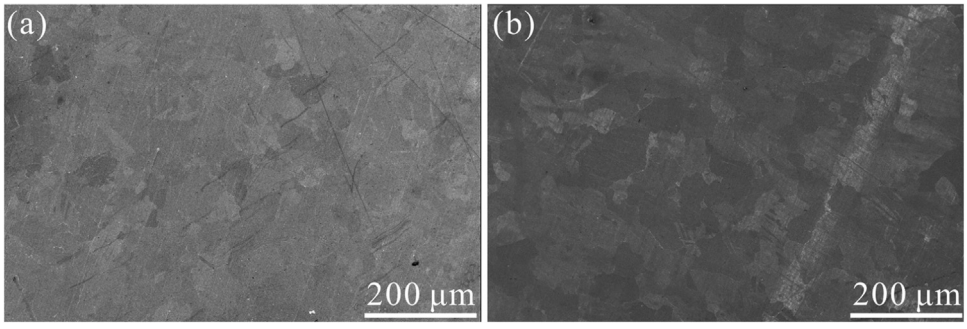

Fig. 11. SEM images of Zn samples after immersed in r-SBF and removal of corrosion product: (a) 48 h and (b) 336 h.

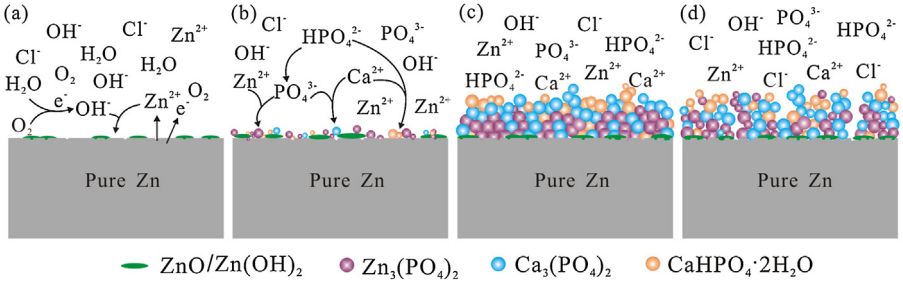

Fig. 12. Schematic illustration of corrosion process of pure Zn immersed in r-SBF solution: (a) the dissolution of Zn and formation of $ZnO/Zn(OH)_2$ at initial stage during immersion; (b) the nucleation of zinc phosphate and calcium phosphates by extending the immersion time; (c) the growth of phosphates and thickening of the corrosion products; (d) partially dissolution of the corrosion product.

observed in the zinc wires *in vivo* before endothelialization [54]. The lack of localized corrosion in this work may be due to the short immersion time. However, it is worth noting that the initial formation of corrosion products was studied in more details in this work, and the components were almost identical to that characterized in the *in vivo* tests. It is reasonable to assume that the r-SBF is suitable for studying the corrosion behavior of pure Zn as stent materials. Nevertheless, the long-term immersion tests should be carried out to better understand the basic corrosion processes underpinning Zn bioabsorption.

4.3. Corrosion mechanism

According to the results interpreted in previous sections, the corrosion mechanism of pure Zn in r-SBF is proposed in Fig. 12. Firstly, the pure Zn corroded through the reactions (Fig. 12(a)):

$$\text{Anodicreaction}: Zn \rightarrow Zn^{2+} + 2e^- \quad (4)$$

$$\text{Cathodicreaction}: O_2 + H_2O + 4e^- \rightarrow 4OH^- \quad (5)$$

$$2H_2O + 2e^- \rightarrow 2OH^- + H_2 \quad (6)$$

In this stage, the dominance of pure Zn dissolution leads to an increase in the corrosion rate CR_i as derived from PDP curves. However, the Pourbaix diagram for Zn shows that zinc has a tendency to be passivated under neutral or slightly alkaline conditions. With the generation of OH^- in the solution, the released Zn^{2+} ion was transformed into $Zn(OH)_2$, parts of which were likely dehydrated to form ZnO [56]:

$$Zn^{2+} + 2OH^- \rightarrow Zn(OH)_2 \quad (7)$$

$$Zn(OH)_2 \rightarrow ZnO + H_2O \quad (8)$$

As depicted in Fig. 12(b), the formation of zinc oxide could promote the nucleation of the phosphate compounds. The $Zn_3(PO_4)_2$, with a low solubility product constant, precipitated preferentially due to the large amount of released Zn^{2+} ions near the surface. On the other hand, the Gibbs free energy, ΔG of the $Zn_3(PO_4)_2$ and $Ca_3(PO_4)_2$ at $37 \pm 0.1\,^{\circ}C$ were calculated to be around $-199.05\,kJ\,mol^{-1}$ and $-198.24\,kJ\,mol^{-1}$, respectively [57]. This indicates that both substances can simultaneously precipitate on the surfaces. At the same time, $HPO_4{}^{2-}$ reacted with Ca^{2+} and subsequently the $CaHPO_4{\cdot}2H_2O$ began to nucleate:

$$HPO_4^{2-} + OH^- \rightarrow PO_4^{3-} + H_2O \quad (9)$$

$$3Zn^{2+} + 2PO_4^{3-} \rightarrow Zn_3(PO_4)_2 \quad (10)$$

$$3Ca^{2+} + 2PO_4^{3-} \rightarrow Ca_3(PO_4)_2 \quad (11)$$

$$Ca^{2+} + HPO_4^{2-} + 2H_2O \rightarrow CaHPO_4 \cdot 2H_2O \quad (12)$$

The phosphates particles continued to grow with prolonged immersion time (Fig. 5(d–h)). As a result, the sample surfaces were covered by a protective layer of corrosion products (Figs. 6 and 12(c)). Simultaneously, the dissolution of Zn decreased, resulting in the release of less Zn^{2+} ions from the samples and less OH^- ions in the solution. Thus, a lower corrosion rate was observed at 168 h (Table 5). As illustrated in Fig. 10(b), a plateau in Zn^{2+} release was observed after 168 h because of the consumption of Zn^{2+} and the decreased corrosion rate. However, the weight loss continuously increased with the immersion time (Fig. 10(c)). The equilibrium was nearly established between the dissolution of Zn and the formation of corrosion products after immersion for 168 h. Besides, it was easier for the $Ca_3(PO_4)_2$ and $CaHPO_4{\cdot}2H_2O$ to form due to the reduced amount of Zn^{2+} in the solutions. As shown in Table 4 and Fig. 8(e), the content of Ca element as well as $Ca_3(PO_4)_2$ and $CaHPO_4{\cdot}2H_2O$ in the corrosion products increased continuously with time. Abundant calcium phosphate compounds formed on the top surface of the corrosion layer during the immersion as discussed in Section 3.2.3.

However, with the accumulation of corrosion products on the sample surface, the likeness of stress concentration in the layer of corrosion products might resulte in the appearance of cracks (Figs. 5(h) and 12(d)). The cracks provided transport paths for the corrosive species, resulting in an insufficient protection for the substrate. Simultaneously, the Cl^- ions from r-SBF attacked the corrosion products, such as zinc hydroxide as follows:

$$Zn(OH)_2 + 2Cl^- \rightarrow Zn^{2+} + 2OH^- + 2Cl^- \quad (13)$$

Partial dissolution of corrosion products cannot protect the Zn substrate effectively, leading to the increase in I_{corr} (Fig. 2(b)) and decrease in R_t (Fig. 3(d)) with the immersion course after 240 h. In addition, a slight increase in the Zn^{2+} concentration was observed after 240 h in Fig. 10(b).

5. Conclusion

The initial corrosion rate and corrosion products of the pure Zn in r-SBF have been investigated to obtain the degradation profile. The electrochemical tests showed that the CR_i fluctuated at each immersion point due to the formation and dissolution of corrosion products during the immersion. However, in the immersion test, the pure Zn displayed uniform corrosion with an estimated corrosion rate of 0.02–0.07 mm y^{-1} during the soaking for 336 h. The corrosion products mainly consisted of $Zn_3(PO_4)_2$ and $Zn(OH)_2/ZnO$ close to the substrate and $Ca_3(PO_4)_2$ and $CaHPO_4{\cdot}2H_2O$ on the top surface of the corrosion layer. The observed corrosion rate and corrosion products support the usage of pure Zn in biomedical application.

Acknowledgements

This work was financially supported by the National Natural Science Foundation of China (Grant Nos. 51503014 and No. 51501008)

and the State Key Laboratory for Advanced Metals and Materials (No. 2016Z-03).

References

[1] A. Purnama, H. Hermawan, J. Biomater. Tissue Eng. 4 (2014) 868–874.
[2] H. Li, Y. Zheng, L. Qin, Prog. Nat. Sci. Mater. 24 (2014) 414–422.
[3] P.K. Bowen, J. Drelich, J. Goldman, Adv. Mater. 2577 (2013) 2577–2582.
[4] N.S. Murni, M.S. Dambatta, S.K. Yeap, G.R. Froemming, H. Hermawan, Mater. Sci. Eng. C 49 (2015) 560–566.
[5] C.J. Frederickson, J.Y. Koh, A.I. Bush, Nat. Rev. Neurosci. 6 (2005) 449–462.
[6] H.F. Li, X.H. Xie, Y.F. Zheng, Y. Cong, F.Y. Zhou, K.J. Qiu, X. Wang, S.H. Chen, L. Huang, L. Tian, Sci. Rep. 5 (2015) 10719.
[7] J.H. Weiss, S.L. Sensi, J.Y. Koh, Trends Pharmacol. Sci. 21 (2000) 395–401.
[8] P.K. Bowen, E.R. Shearier, S. Zhao, F. Zhao, J. Goldman, J.W. Drelich, Adv. Healthcare Mater. 5 (2016) 1121.
[9] B. Hennig, M. Toborek, C.J. Mcclain, Nutrition 12 (1996) 711–717.
[10] T.A. Ostomel, Q.H. Shi, P.K. Stoimenov, G.D. Stucky, Langmuir 23 (2012) 11233–11238.
[11] Y.H. Cheng, B. Liu, Y.H. Wu, Y.F. Zheng, J. Mater. Sci. Technol. 29 (2013) 619–627.
[12] J. Kubásek, D. Vojtěch, E. Jablonská, I. Pospíšilová, J. Lipov, T. Ruml, Mater. Sci. Eng. C 58 (2016) 24–35.
[13] H.F. Li, H.T. Yang, Y.F. Zheng, F.Y. Zhou, K.J. Qiu, X. Wang, Mater. Des. 83 (2015) 95–102.
[14] E. Mostaed, M. Sikorajasinska, A. Mostaed, S. Loffredo, A.G. Demir, B. Previtali, D. Mantovani, R. Beanland, M. Vedani, J. Mech. Behav. Biomed. 60 (2016) 581–602.
[15] Z.Z. Shi, J. Yu, X.F. Liu, L.N. Wang, J. Mater. Sci. Technol. 34 (2018) 1008–1015.
[16] Y. Chen, W. Zhang, M.F. Maitz, M. Chen, H. Zhang, J. Mao, Y. Zhao, N. Huang, G. Wan, Corros. Sci. 111 (2016) 541–555.
[17] X. Liu, J. Sun, Y. Yang, Z. Pu, Y. Zheng, Mater. Lett. 161 (2015) 53–56.
[18] K. Törne, M. Larsson, A. Norlin, J. Weissenrieder, J. Biomed. Mater. Res. B 104 (2015) 1141–1151.
[19] T. Kokubo, H. Takadama, Biomaterials 27 (2006) 2907–2915.
[20] A. Yamamoto, S. Hiromoto, Mater. Sci. Eng. C 29 (2009) 1559–1568.
[21] B.J. Wang, D.K. Xu, J.H. Dong, W. Ke, J. Mater. Sci. Technol. 32 (2016) 646–652.
[22] A. Miklaszewski, M.U. Jurczyk, M. Jurczyk, J. Mater. Sci. Technol. 29 (2013) 565–572.
[23] M.I. Jamesh, G. Wu, Y. Zhao, D.R. McKenzie, M.M.M. Bilek, P.K. Chu, Corros. Sci. 91 (2015) 160–184.
[24] N.I. Zainal Abidin, D. Martin, A. Atrens, Corros. Sci. 53 (2011) 862–872.
[25] C. Wang, Z.T. Yu, Y.J. Cui, Y.F. Zheng, S. Yu, G.Q. Qu, H.B. Gong, J. Mater Sci. Technol. 32 (2016) 925–929.
[26] ISO 8407:2009 (E), International standard ISO 8407, 2nd ed., 2009.
[27] H. Ibrahim, A.D. Klarner, B. Poorganji, D. Dean, A.A. Luo, M. Elahinia, J. Mech. Behav. Biomed. 69 (2017) 203–212.
[28] ASTM Standard G1-03, Annual Book of ASTM Standards, vol. 03.02, ASTM, Philadelphia, PA, 2011, pp. 2011.
[29] H.X. Wang, Y.W. Song, J. Yu, D.Y. Shan, E.N. Han, J. Electrochem. Soc. 164 (2017) C574–C580.
[30] J.H. Liu, Y.W. Song, D.Y. Shan, E.H. Han, J. Electrochem. Soc. 163 (2016) C856–C863.
[31] L.J. Liu, P.P. Li, Y.H. Zou, K.J. Luo, F. Zhang, R.C. Zeng, S.Q. Li, Surf. Coat. Technol. 291 (2016) 7–14.
[32] Y.C. Su, L.Y. Niu, Y.B. Lu, J.S. Lian, G.Y. Li, J. Electrochem. Soc. 160 (2013) C536–C541.
[33] E.T. Heakal, A.M. Fekry, A.A. Ghoneim, Corros. Sci. 50 (2008) 1618–1626.
[34] Z.M. Shi, M. Liu, A. Atrens, Corros. Sci. 52 (2010) 579–588.
[35] R.C. Zeng, X.T. Li, L.J. Liu, S.Q. Li, F. Zhang, J. Mater. Sci. Technol. 32 (2016) 437–444.
[36] K.K. Li, B. Wang, B. Yan, W. Lu, J. Biomater. Appl. 28 (2012) 375–384.
[37] G.Y. Liu, J. Hu, Z.K. Ding, C. Wang, Appl. Surf. Sci. 257 (2011) 2051–2057.
[38] P.K. Bowen, J. Drelich, J. Goldman, Acta Biomater. 10 (2014) 1475–1483.
[39] S.K.F. Asl, S. Nemeth, M.J. Tan, Surf. Coat. Technol. 258 (2014) 931–937.
[40] A. Anwar, S. Akbar, A. Sadiqa, M. Kazmi, Inorg. Chim. Acta 453 (2016) 16–22.
[41] E.C. Onyiriuka, J. Non-Cryst. Solids 163 (1993) 268–273.
[42] T. Hanawa, M. Ota, Biomaterials 12 (1991) 767–774.
[43] S.Z. Khalajabadi, M.R.A. Kadir, S. Izman, M. Marvibaigi, J. Alloys Compd. 655 (2016) 266–280.
[44] B. Ramezanzadeh, H. Vakili, R. Amini, Appl. Surf. Sci. 327 (2015) 174–181.
[45] C.D. Wagner, W.M. Riggs, L.E. Davis, J.F. Moulder, G.E. Muilenbery, Handbook of X-Ray Photoelectron Spectroscopy, Perkin-Elmer Corporation, Physical Electronics Division, Eden Prairie, Minn, 1979, p. 55344.
[46] C.Y. Tsai, J.S. Liu, P.L. Chen, C.S. Lin, Corros. Sci. 52 (2010) 3385–3393.
[47] S. Karimi, T. Nickchi, A. Alfantazi, Corros. Sci. 53 (2011) 3262–3272.
[48] D. Vojtěch, J. Kubásek, J. Serák, P. Novák, Acta Biomater. 7 (2011) 3515–3522.
[49] Z.B. Tang, J.L. Niu, H. Huang, H. Zhang, J. Pei, J.M. Ou, G.Y. Yuan, J. Mech. Behav. Biomed. 72 (2017) 182–191.
[50] A.J. Drelich, P.K. Bowen, L. Lalonde, J. Goldman, J.W. Drelich, Surf. Innov. 4 (2016) 1.
[51] Y.C. Xin, P.K. Chu, Mater. Chem. Phys. 124 (2010) 33–35.
[52] S.Y. Zhang, Y. Zheng, L.M. Zhang, Y.Z. Bi, J.Y. Li, J. Liu, Y.B. Yu, H.Q. Guo, Y. Li, Mater. Sci. Eng. C 68 (2016) 414–422.
[53] H. Kalb, A. Rzany, B. Hensel, Corros. Sci. 57 (2012) 122–130.
[54] J. Yang, C.D. Yim, B.S. You, J. Electrochem. Soc. 163 (2016) C839–C844.
[55] A.J. Drelich, S. Zhao, R.J. Guillory, J.W. Drelich, J. Goldman, Acta Biomater. 58 (2017) 539–549.
[56] J. Yang, C.D. Yim, B.S. You, J. Electrochem. Soc. 163 (2016) C839–C844.
[57] R.C. Zeng, Z.D. Lan, L.H. Kong, Y. Huang, H. Cui, Surf. Coat. Technol. 205 (2011) 3347–3355.